AGU ADVANCING EARTH AND SPACE SCIENCE

Water Resources Research

RESEARCH ARTICLE
10.1029/2020WR029125

Upscaling Reactive Transport and Clogging in Shale Microcracks by Deep Learning

Ziyan Wang[1] and **Ilenia Battiato**[1]

[1]Stanford University, Energy Resources Engineering, Stanford, CA, USA

Key Points:

- We propose a hybrid framework for modeling reactive transport and clogging in multiscale fracture networks
- Microcracks are upscaled by deep learning while main fractures are described by theory-based modeling, ensuring a two-way coupling
- The framework provides a reliable and efficient upscaling method without relying on the existence of macroscopic equations

Correspondence to:
I. Battiato,
ibattiat@stanford.edu

Citation:
Wang, Z., & Battiato, I. (2021). Upscaling reactive transport and clogging in shale microcracks by deep learning. *Water Resources Research*, *57*, e2020WR029125. https://doi.org/10.1029/2020WR029125

Received 28 OCT 2020
Accepted 19 MAR 2021

Abstract Fracture networks in shales exhibit multiscale features. A rock system may contain a few main fractures and thousands of microcracks, whose length and aperture are orders of magnitude smaller than the former. It is computationally prohibitive to resolve all the fractures explicitly for such multiscale fracture networks. One traditional approach is to model the small-scale features (e.g., microcracks in shales) as an effective medium. Although this fracture-matrix conceptualization significantly reduces the problem complexity, there are classes of physical processes that cannot be accurately upscaled by effective medium approximations, for example, microcrack clogging during mineral reactions. In this work, we employ deep learning in place of effective medium theory to upscale physical processes in small-scale features. Specifically, we consider reactive transport in a fracture-microcrack network where microcracks can be clogged by precipitation. A deep learning multiscale algorithm is developed, in which the microcracks are upscaled as a wall boundary condition of the main fractures. The wall boundary condition is constructed by recurrent neural networks, which take concentration histories as input and predict the solute transport from main fractures to microcracks. The deep learning multiscale algorithm is first employed in specific scenarios, then a general model is developed which can work under various conditions. The new approach is validated against fully resolved simulations and an analytical solution, providing a reliable and efficient solution for problems that cannot be upscaled by effective medium models.

1. Introduction

To economically recover the unconventional hydrocarbons stored in shales, the formation needs to be stimulated because of its ultralow permeability. This is accomplished by hydraulic fracturing, which consists in injecting a large amount of water-based fluid at high pressure and fracturing the formation. The fracking fluid usually contains a number of chemicals which can react with minerals in shales, causing dissolution or precipitation (Entrekin et al., 2011; Paukert Vankeuren et al., 2017). Recently, precipitation has become a major concern for hydraulic fracturing operators (Vidic et al., 2013). To curb the impact on water resources, the wastewater from previous fracturing operations is commonly reused after dilution or pretreatment (e.g., in Pennsylvania) (Maloney & Yoxtheimer, 2012). It is important to understand what level of water treatment must be achieved for reuse, so that precipitation would not severely impair formation permeability through clogging (Vidic et al., 2013). Reactive transport modeling can help to evaluate the impact of precipitation on fracture network conductivity and determine the minimum treatment for the wastewater, reducing the costs for fracturing operations (Paukert Vankeuren et al., 2017).

Solute transport and reaction in fractured and porous media have been widely investigated in water contamination (B. Guo et al., 2020; Molson et al., 2012; Yeh et al., 2010) and nuclear waste disposal (Fleming & Haggerty, 2001; Haggerty et al., 2001). An emerged challenge in modeling reactive transport in fractured shales is the multiscale nature of the fracture network. Observations on core samples show that there are a large number of microcracks in shales (Ougier-Simonin et al., 2016) of aperture ranging from a few to tens of micrometers. These are much smaller than the main fractures induced by hydraulic fracturing operations. Recent experiments have revealed that the microcracks can be entirely clogged by precipitation, blocking the pathways from matrix to main fractures in hydrocarbon recovery (Alalli et al., 2018; Q. Li et al., 2018). Pore-scale modeling can accurately capture precipitation in single fractures (X. Li et al., 2008) and submillimeter fracture networks in shales (Soulaine & Tchelepi, 2016). However, as the number of fractures increases, explicitly resolving all the fractures can be computationally prohibitive because of the nonlinear scaling of computational costs with fracture number.

Upscaling is commonly adopted to address the multiscale problem. In upscaling, small-scale features are described by a model that can be incorporated in large-scale problems. One traditional approach is to model small-scale features as an effective medium (Battiato et al., 2019): this can be accomplished by the homogenization method (Hornung, 1996), the volume averaging method (Whitaker, 2013), statistic modeling (Kröner, 1986), etc. After upscaling, a fractured medium can be conceptualized as a fracture-matrix system, where solute transport in different domains is governed by different physics (e.g., the multirate diffusion model) (Haggerty et al., 2001). However, there are physical processes that cannot be accurately upscaled by effective medium models. For example, precipitation and dissolution in fractures may lead to nonperiodic geometry that cannot be homogenized, which requires pore-scale modeling to capture (X. Li et al., 2008; Soulaine & Tchelepi, 2016). In addition, macroscopic governing equations in the form of standard advection-reaction-dispersion equations may not exist unless a number of restrictions are satisfied (Battiato & Tartakovsky, 2011; Boso & Battiato, 2013).

Data-driven approaches have recently been adopted to upscale flow and transport in porous media and fracture networks. Among the data-driven models, deep learning has gained widespread acceptance due to its accuracy and flexibility in handling different types of problems (Karpatne et al., 2017). First, deep learning models with the architecture of convolutional neural networks can determine upscaled coefficients (e.g., permeability and effective diffusivity) directly from pore-scale images, without solving a complex closure problem (Kamrava et al., 2020; Santos et al., 2020; Wu et al., 2019). Second, deep learning can replace the effective medium model by directly predicting the responses from small-scale features under different conditions. For example, neural networks can predict behaviors of an electrode structure under various battery operating conditions (Bao et al., 2020), and forecast oil production from fractured shales without solving the macroscopic Darcy's equation (Klie & Florez, 2018).

However, there are two major limitations in data driven modeling of physical processes: one is that the model may not generalize well outside the available data set; the other is that the model may not be interpretable. To overcome these limitations, a paradigm of theory-guided data science has been proposed, which introduces physical knowledge in data driven modeling (Karpatne et al., 2017). The paradigm has shown promise in many scientific disciplines and recently been applied in water resources modeling (Fleming & Goodbody, 2019; Khandelwal et al., 2017). In this work, we propose a hybrid framework, in which reactive transport in small-scale features is upscaled by deep learning, while in large-scale features theory-based modeling is adopted. The deep learning provides boundary conditions for the theory-based modeling, while the theory-based modeling provides input variables for the deep learning, establishing a two-way coupling between small-scale and large-scale features. In the framework, the upscaling is performed without relying on the existence of macroscopic equations, and the deep learning model shows capability for generalization beyond the available data set.

The manuscript is organized as follows. In Section 2 and 3, we present the physical model and the deep learning multiscale algorithm. The validation of the algorithm and the results with fracture clogging are presented in Section 4. Section 5 contains the conclusions and discussions of this work.

2. Physical Model

We consider flow of an incompressible Newtonian fluid and transport of a reactive solute in a multiscale fracture network (Figure 1). The network is constituted by eight main fractures and 972 microcracks. There are three main fractures in the horizontal direction and the rest are connected at 75°, which is designed based on hydraulic fracturing experiments (Figure 2a of T. Guo et al., 2014). To represent fracture aperture variations observed in the experiments, the horizontal main fracture in the middle and the first and third tilted main fractures, counted from the left, are twice as wide as the other main fractures. For microcracks, the design is based on synchrotron X-ray microtomography views of shales (Figure 2b of Ougier-Simonin et al., 2016) and Scanning Electron Microscopy (SEM) shale images (Alalli et al., 2018). Geometric parameters of the fracture network are listed in Table 1. The idealized fracture network is purposefully 2D to ensure that fully resolved pore-scale simulations are still feasible for model validation in such a severely multiscale domain. It is worth emphasizing that shales present additional structural and chemical complexity compared to the benchmark model used in this study.

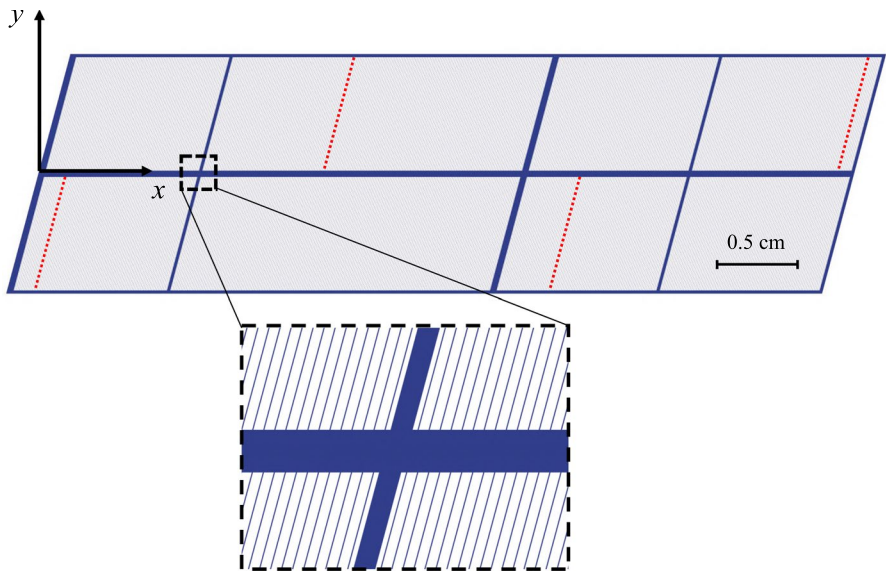

Figure 1. The multiscale fracture network in which flow and reactive transport are modeled. The fracture network contains eight main fractures and 972 microcracks, where a microcrack is defined as a segment connecting two main fractures. The red dotted lines mark the microcracks selected for test set generation.

Pore-scale equations are employed in both main fractures and microcracks. Specifically, fluid flow is described by the incompressible Navier-Stokes equations:

$$\nabla \cdot \mathbf{u} = 0, \tag{1a}$$

$$\frac{\partial \mathbf{u}}{\partial t} + (\mathbf{u} \cdot \nabla)\mathbf{u} - \nu \nabla^2 \mathbf{u} = -\frac{\nabla p}{\rho}, \tag{1b}$$

where $\mathbf{u}(\mathbf{x}, t) = (u(\mathbf{x}, t), v(\mathbf{x}, t), w(\mathbf{x}, t))$, $p(\mathbf{x}, t)$, ρ, and ν are the fluid's velocity, pressure, density, and kinematic viscosity, respectively. Solute transport is described by the advection-diffusion equation:

$$\frac{\partial c}{\partial t} = D\nabla^2 c - \nabla \cdot (\mathbf{u}c), \tag{2}$$

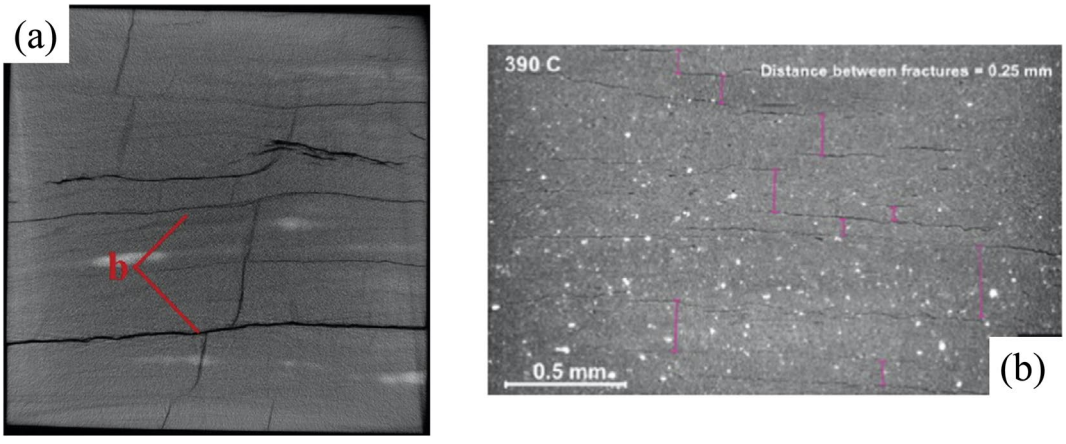

Figure 2. (a) A 30× 30 cm computer tomography (CT) image of the fracture network in shales after hydraulic fracturing experiment (T. Guo et al., 2014). (b) A synchrotron X-ray microtomography view of microcracks, generated by gas production during the maturation of organic matter (Ougier-Simonin et al., 2016).

Table 1
Geometric Parameters of the Fracture Network

Geometric parameters	Length (mm)
Horizontal main fracture length (L)	51.76
Fracture network width (W)	15.2
Main fracture aperture (H)	0.2, 0.4
Microcrack aperture (h)	0.01
Distance between microcracks (d)	0.1

where c and D are the concentration and diffusivity of the solute, respectively.

At fluid-solid interfaces, the solute undergoes a heterogenous reaction and precipitates on the interfaces (X. Li et al., 2010; Mourzenko et al., 1996):

$$-\mathbf{n}\cdot(D\nabla c-\mathbf{u}c)=Kc, \tag{3a}$$

$$-\mathbf{n}\cdot\mathbf{u}=KcV, \tag{3b}$$

$$\mathbf{t}\cdot\mathbf{u}=0, \tag{3c}$$

where K is the reaction rate constant on the fluid-solid interfaces, V the molar volume of the precipitate, $\mathbf{n}$ the outward unit normal vector and $\mathbf{t}$ the unit tangential vector. Since microcracks are easier to be clogged and have much larger fluid-solid interface than main fractures (see geometric parameters in Table 1 for quantitative comparison), we focus on reactions in microcracks by assuming $K=0$ on the main fracture walls. The initial condition for concentration is set to

$$c(\mathbf{x},t=0)=0, \tag{4}$$

while the flow is assumed to have already reached steady state when the solute is injected. This hypothesis is consistent with the observation that flow reaches steady state much faster than transport. We note that in the reactive transport modeling, the mechanical propagation of fractures is not considered. The system can be viewed as a domain that has been fractured, but fluid is continuously injected for fracking other regions. The presence of hydrocarbons is also not considered, assuming they do not significantly affect reactive transport.

3. Upscaling by Deep Learning

In traditional upscaling approaches, small-scale features are usually represented by an effective medium, which needs to be resolved explicitly through the solution of macroscopic equations. In the upscaling method we developed with deep learning, only large scale features, for example, main fractures, are explicitly resolved. All responses from small-scale features are predicted by neural networks based on the state of large-scale features. Since the system evolves with time, both the input and the output of the neural networks are time-series data, which can be well handled by the recurrent neural network (RNN) model. Specifically, the RNN takes concentration histories (i.e., concentration breakthrough curves) on the main fracture walls as input and predicts the solute mass flux histories on the walls, that is, the diffusive transport from the main fractures to the microcracks. Advective transport in microcracks is currently neglected because it is much weaker than the diffusive transport due to their size. A flowchart of the algorithm is presented in Figure 3, with details described in the following Sections.

3.1. Recurrent Neural Networks

We employ RNN to model solute transport between main fractures and microcracks. Since each microcrack connects two main fractures, two RNNs are constructed to capture solute transport at the two ends of a microcrack, respectively. We define an end of a microcrack as the inlet, if it is closer to the fracture network inlet, and define the other end as the outlet. Although there may be complex physical and chemical processes inside microcracks, mass fluxes at the inlet and outlet are uniquely determined by the inlet and outlet concentration boundary conditions. Thus, RNN can predict the mass flux at the inlet or outlet by taking both the inlet and outlet concentration as input. We emphasize that the mass flux of the solute is superficially averaged the same way as in effective medium theories, that is,

$$f=\frac{F}{d\ /\ sin(\theta)}, \tag{5}$$

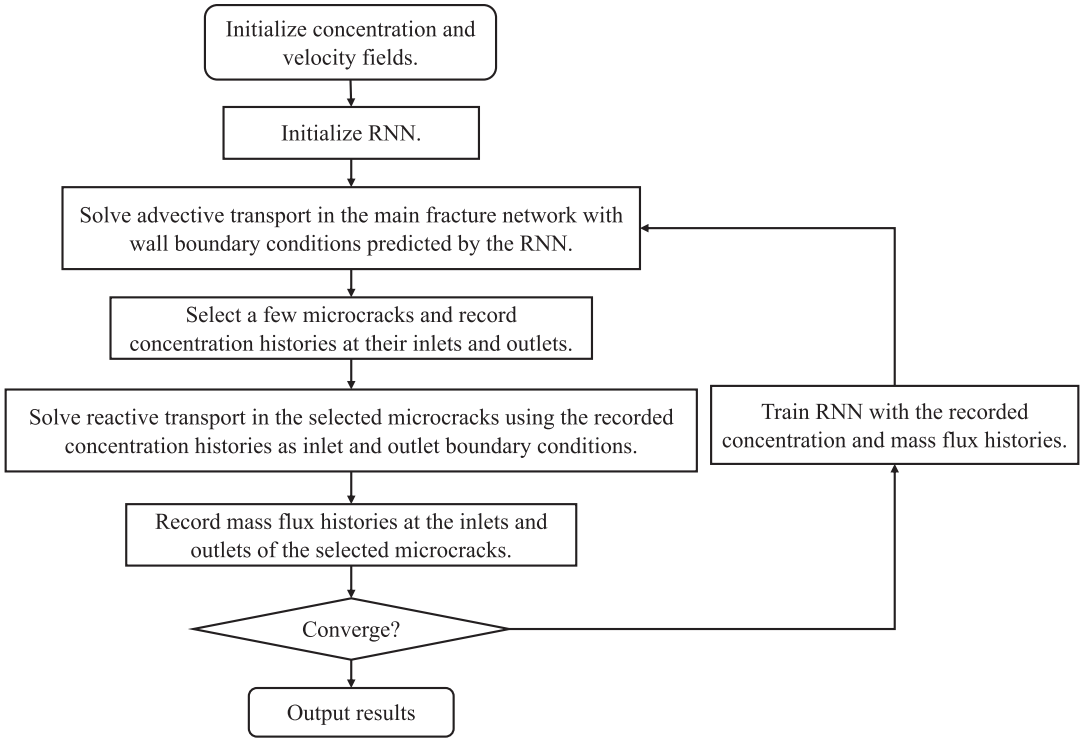

Figure 3. The flowchart of the upscaling algorithm by deep learning. More detailed explanation of each step is given in Section 3.2.

where F is the mass flow rate of the solute at the microcrack inlet or outlet, d the distance between microcracks, and θ the connection angle.

Since both the concentration and mass flux are time dependent, the RNN input is constituted by two-time series (concentration histories at the inlet and outlet) and the RNN output is one-time series (mass flux history at the inlet or outlet). The RNN contains one input layer, one output layer, and several hidden layers (Figure 4). The input layer has two nodes for the inlet and outlet concentration time series; the output has one node for the inlet or outlet mass flux series; and there are n hidden layers with m nodes in each layer. The hidden layers are computed following the popular RNN architecture long short-term memory (LSTM) (Hochreiter & Schmidhuber, 1997), while the output layer is computed by a linear transformation of the data in the last hidden layer.

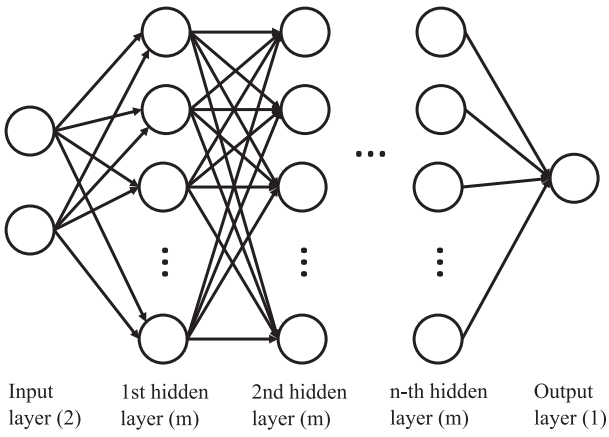

Figure 4. A schematic representation of the recurrent neural network (RNN) structure. For cases without clogging: $m = 51$, $n = 2$; for the clogging case: $m = 204$, $n = 4$.

The RNN is implemented by PyTorch, where a built-in function LSTM Cell is adopted to compute the nodes in the hidden layers. To train the RNN, we choose the L-BFGS optimizer (Liu & Nocedal, 1989), since the training set is relatively small and we can load the whole data set to train. The optimizer works through the entire data set a number of times (number of epochs), updating the internal parameters of RNN to reduce the loss function, which is defined by mean squared error. The RNN is designed and trained differently for cases with and without microcrack clogging because of the different complexity in physics. For the cases without clogging, the RNN contains two hidden layers with 51 nodes in each layer. The number of epochs is 30 and the learning rate is 0.2. For the clogging case, there are four hidden layers with 204 nodes in each layer, and the RNN is trained with 300 epochs and 0.05 learning rate. The number of epochs is fixed without early stopping techniques because overfitting is not significant.

3.2. Multiscale Modeling

We propose a hybrid framework for modeling reactive transport in multiscale fracture networks. The microcracks are upscaled by RNN as a wall boundary condition of the main fractures, while the main fractures are discretized and solved by traditional finite volume method. As demonstrated in the flowchart (Figure 3), the multiscale modeling framework has the following steps:

Step 1 *System initialization*. We start the multiscale modeling by initializing the concentration and velocity fields. Note that only the main fracture network is explicitly resolved and only initial conditions in main fractures are required as a result. The concentration field is initialized as zero, while the velocity field is set to be at steady state.

Step 2 *RNN initialization*. Since no training data is available yet, the RNN is set to always give zero as output. This corresponds to a case with no solute transport in microcracks.

Step 3 *Modeling in the main fracture network*. Our objective is to solve the concentration field at time t^{n+1} using the information from t^0 to t^n. The velocity field is not updated since it is already at steady state. On main fracture walls, a mass flux wall boundary condition is employed, which represents the solute transport from main fractures to microcracks. At any location $\mathbf{x}$ on main fracture walls, the wall boundary condition is constructed as follows:

Step 3.1 Find a partner location $\mathbf{x}'$ such that $\mathbf{x}$ and $\mathbf{x}'$ are connected by a microcrack. Without loss of generality, we assume $\mathbf{x}$ corresponds to the inlet of that microcrack. If $\mathbf{x}$ is located in gaps between microcracks, use interpolation to find $\mathbf{x}'$. If $\mathbf{x}$ is located on walls that are not connected by microcracks, set the wall boundary condition to be no mass flux.

Step 3.2 Next we compute the current mass flux at $\mathbf{x}$ based on the concentration histories at $\mathbf{x}$ and $\mathbf{x}'$. The concentration histories, $c(\mathbf{x}, t^0)$, $c(\mathbf{x}', t^0)$; $c(\mathbf{x}, t^1)$, $c(\mathbf{x}', t^1)$; ...; $c(\mathbf{x}, t^n)$, $c(\mathbf{x}', t^n)$, are already computed in previous time steps. The inlet and outlet concentration time series, $\{c(\mathbf{x}, t^i)\}$ and $\{c(\mathbf{x}', t^i)\}$, are fed into RNN to predict the current mass flux at $\mathbf{x}$: $f(\mathbf{x}, t^n)$.

Step 3.3 Obtain the concentration field at t^{n+1} using the concentration field at t^n as initial condition and mass flux $f(\mathbf{x}, t^n)$ as wall boundary condition.

Step 3.4 The concentration field in Step 3.3 is computed explicitly. To improve accuracy, an implicit algorithm is employed: We feed the RNN with concentration time series, $c(\mathbf{x}, t^0)$, $c(\mathbf{x}', t^0)$; $c(\mathbf{x}, t^1)$, $c(\mathbf{x}', t^1)$; ...; $c(\mathbf{x}, t^{n+1})$, $c(\mathbf{x}', t^{n+1})$, to predict mass flux $f(\mathbf{x}, t^{n+1})$, then obtain the concentration field at t^{n+1} implicitly with $f(\mathbf{x}, t^{n+1})$ as wall boundary condition. Iterate until the concentration field at t^{n+1} has converged.

Step 4 *Recording concentration history*. We uniformly select a few microcracks and mark the locations of their inlets and outlets on main fracture walls, then record the concentration histories at the marked locations.

Step 5 *Modeling in each selected microcrack*. The governing Equation 2 with reactive wall boundary conditions, Equation 3, is solved in a single microcrack. The velocity field in Equation 2 is set to zero because the advective transport in microcracks can be neglected, and the concentration field is initialized as zero. A number of simulations are performed independently, with each corresponding to one of the selected microcracks in Step 4. The recorded concentration histories serve as inlet and outlet boundary conditions in the simulations.

Step 6 *Recording mass flux history*. Based on results from Step 5, the mass flux histories at the inlets and outlets of the selected microcracks are recorded.

Step 7 *RNN training*. We train new RNN with the recorded concentration and mass flux histories. Go back to Step 3 with the updated RNN until the concentration and mass flux histories have converged.

There are several simplifications in the multiscale algorithm proposed here. First, the microcracks are assumed to be geometrically identical. To generalize the algorithm to microcracks with varying apertures and lengths, geometric parameters such as microcrack length and aperture can serve as additional features in neural networks using data fusion techniques (Castanedo, 2013). Second, advection in microcracks is neglected, which can be modeled by including pressure histories on the main fracture walls, following a similar procedure. Third, solute transport between microcracks is neglected by assuming the microcracks do not intersect with each other. More complex microcrack morphology can be introduced by training RNN based on simulations in submillimeter fracture networks (Soulaine & Tchelepi, 2016). We emphasize that

Table 2
Modeling Parameters in the Simulations

Modeling parameters	Value
Diffusivity (D, m^2/s)	1×10^{-9}
Kinematic viscosity (ν, m^2/s)	1×10^{-6}
Inlet concentration (c_{in}, [C])	1
Case 1: Pure diffusion	
Time step (δt, s)	100
Time domain	(0, 50,000 s)
Case 2: Reactive transport	
Time step (δt, s)	10
Time domain	(0, 50,000 s)
Reaction rate constant (K, m/s)	1×10^{-9}
Case 3: Reactive transport with clogging	
Time step (δt, s)	10
Time domain	$[0, 1 \times 10^5$ s]
Reaction rate constant (K, m/s)	5×10^{-9}
Molar volume of the precipitate (V, [1/C])	0.1

although the multiscale algorithm is motivated by reactive transport in shales, the method is applicable for other problems such as mineral deposition in hydrothermal systems and precipitation in water contamination. We also note that the algorithm can work for dead-end microcracks, in which case only one RNN is needed to predict the mass flux at the open end.

The deep learning multiscale algorithm is efficient because pore-scale modeling is performed only on main fractures and a few selected microcracks, which occupy only a small portion of the entire domain. The trade-off is that RNN training can be computationally expensive. To avoid frequent training, we can devise a RNN that can work under various dynamic conditions. As an example, we construct a general model that can work over a wide range of Péclet number (Pe), defined in Equation 9a. We first select a few Pe in the desired range, then solve the corresponding cases using the above algorithm. Combining the results, a broader training set is generated, based on which a general model is constructed. For any new cases in the Pe range, we can utilize the general model directly without RNN training, which makes the deep learning algorithm even more efficient. More details about the general model will be covered in Section 4.2.

4. Results

We employ OpenFOAM to solve the physical model described in Section 2. The steady-state flow field is obtained by a preprocess solver of Equation 1 using PIMPLE algorithm, and the advection-diffusion Equation 2 is solved by finite volume method. The modeling parameters adopted in the following simulations are provided in Table 2. We emphasize that the diffusivity is selected based on the diffusivities of common ions presented in hydraulic fracturing fluid (Parkhurst & Appelo, 2013; Vidic et al., 2013), and the kinematic viscosity is set to that of water.

In Section 4.1, the deep learning multiscale algorithm is first employed to solve a pure diffusion problem in a simplified fracture network with fishbone geometry, which has been investigated in our previous work (Wang & Battiato, 2020). Then reactive transport in a multiscale fracture network is considered in Section 4.2. Section 4.3 includes the modeling of reactive transport with microcrack clogging.

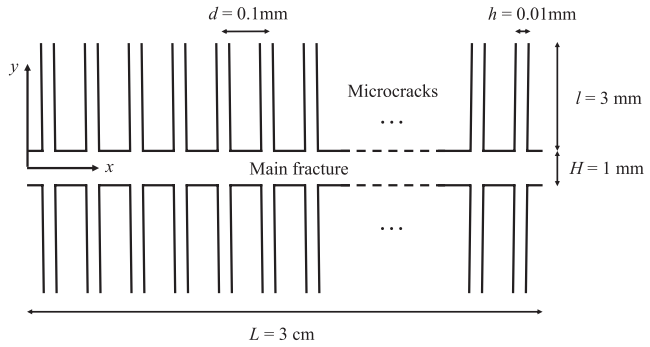

Figure 5. A schematic representation of the simplified fracture system with fishbone geometry, where 600 microcracks are connected to a main fracture. The geometry is adopted in pure diffusion modeling to validate simulations against an analytical solution.

4.1. Pure Diffusion

First, we consider a simplified fracture system with fishbone geometry, where a main fracture is connected to an array of microcracks on each side (Figure 5). We start by modeling pure diffusion without any advection and reaction, in which case an analytical solution exists. Specifically, we take $\mathbf{u} \equiv \mathbf{0}$ in Equation 2 and $K = 0$ in Equation 3, while adopting the following initial and boundary conditions,

$$c(\mathbf{x}, t = 0) = 0, \tag{6a}$$

$$c(x = 0, y, t) = 1, \tag{6b}$$

$$c(x = L, y, t) = 0, \tag{6c}$$

$$c(x, y = H/2 + l, t) = 0, \tag{6d}$$

where Equations 6a, 6b, 6c, and 6d represent the initial condition, the boundary conditions at the main fracture inlet and outlet, and the

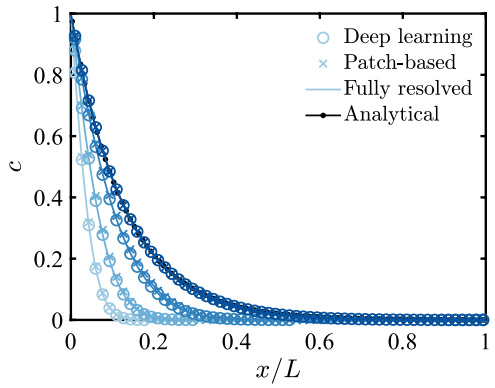

Figure 6. Concentration profiles at the centerline of the fishbone geometry in the pure diffusion problem, computed by the deep learning algorithm (o), the patch-based algorithm (x) (Wang & Battiato, 2020) and the fully resolved simulation (solid line), at time instances 1,000 s, 3,000 s, 10,000 s, and 50,000 s (from light color to dark color). The dotted line is the analytical solution at steady state.

boundary condition at the microcrack outlets, respectively. Since the concentration at the microcrack outlets is fixed at zero, only concentration histories at the microcrack inlets are fed into the RNN to predict the mass flux histories at the inlets. We selected 20 microcracks uniformly along the main fracture to collect training data. The RNN, which contains two hidden layers with 51 nodes in each layer, is constructed and trained in PyTorch.

The deep learning multiscale algorithm is validated against fully resolved simulations and a steady-state analytical solution. To make fully resolved simulations feasible, the number of microcracks is limited to 600, with 300 connected on each side of the main fracture. In addition, only the upper half is modeled in fully resolved simulations due to the symmetric geometry. The main fracture and microcracks are resolved by 300 × 10 and 10 × 300 grid resolution, respectively, in both multiscale and fully resolved simulations. To improve the multiscale modeling efficiency, the mass flux wall boundary is updated every 10 simulation time steps ($t^{n+1} - t^n = 10\delta t$).

Figure 6 presents concentration profiles in the main fracture at different times, computed by the deep learning multiscale algorithm, the fully resolved simulation, and a patch-based multiscale algorithm proposed in our previous work (Wang & Battiato, 2020). Both the deep learning and the patch-based multiscale algorithm agree well with the fully resolved simulation, and all simulation results recover the steady-state analytical solution:

$$\overline{c} = \frac{\sinh[(L-x)\sqrt{2h\,/\,(Hld)}]}{\sinh[L\sqrt{2h\,/\,(Hld)}]}, \tag{7}$$

where $\overline{c}$ is the cross-averaged concentration in the main fracture. This proves the accuracy of our multiscale and fully resolved models. Figure 7 plots the error of the deep learning and patch-based multiscale algorithms, which is defined as the difference between concentration from the multiscale algorithm and fully resolved simulations, normalized by inlet concentration. We emphasize that only one iteration is performed in the deep learning algorithm, and the results are already more accurate than the patch-based algorithm. The reason could be that in the patch-based algorithm, we employ linear interpolation to evaluate gaps between patches, while deep learning can better capture the nonlinearity with neural networks.

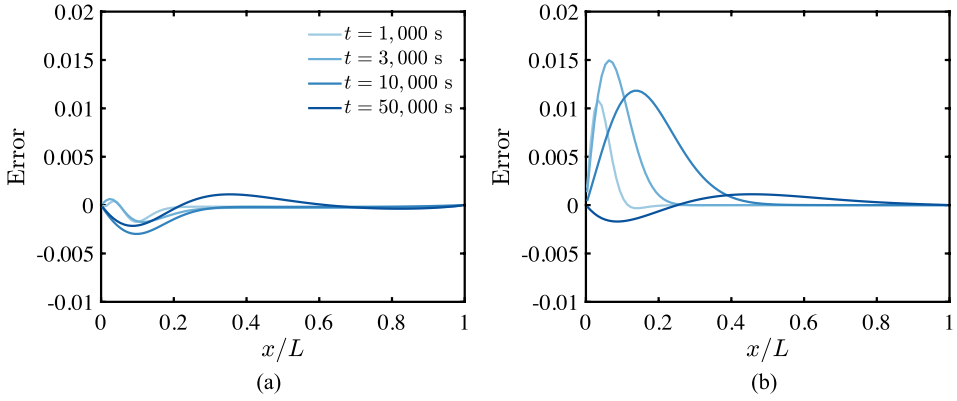

Figure 7. Normalized concentration differences between multiscale modeling and fully resolved simulations in the pure diffusion case: (a) deep learning multiscale modeling; (b) patch-based multiscale modeling (Wang & Battiato, 2020).

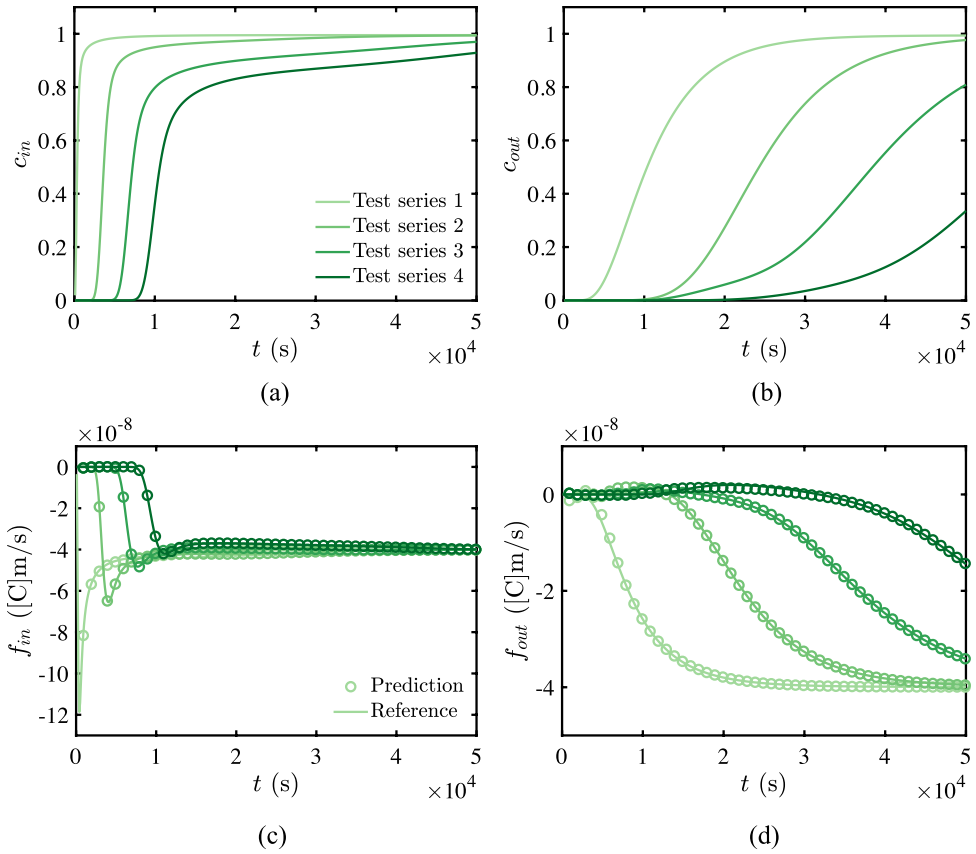

Figure 8. Concentration histories at (a) inlets and (b) outlets of the four microcracks in the test set, whose inlets are located at $x = 1.64$, 17.94, 34.03, 50.33 mm. The corresponding mass flux histories are plotted in (c) and (d), where circles are recurrent neural network (RNN) predictions and solid lines are reference data. The results are obtained without any iterations.

4.2. Reactive Transport

In this section, we solve the advection-reaction-diffusion problem in a multiscale fracture network (Figure 1). We assume the solute consumed in reaction does not cause clogging (e.g., adsorption) and set $V = 0$ in Equation 3. The following initial and boundary conditions are adopted:

$$c(\mathbf{x}, t = 0) = 0, \tag{8a}$$

$$c(x = 0, y = 0, t) = 1, \tag{8b}$$

$$\left.\frac{\partial c}{\partial x}\right|_{x=L, y=0} = 0, \tag{8c}$$

where Equations 8a, 8b and 8c represent the initial condition, the inlet boundary condition and the outlet boundary condition. The velocity field in Equation 2 is set at steady state, which is obtained by solving Equation 1 by a preprocess solver under constant inlet and outlet pressure boundaries.

First, we consider a specific case with $Pe = 3.29$ and $Da = 4 \times 10^{-4}$. The Péclet number (Pe) and Damköhler number (Da) are defined as:

$$Pe = U_m H_m \,/\, D, \tag{9a}$$

$$Da = K H_m \,/\, D, \tag{9b}$$

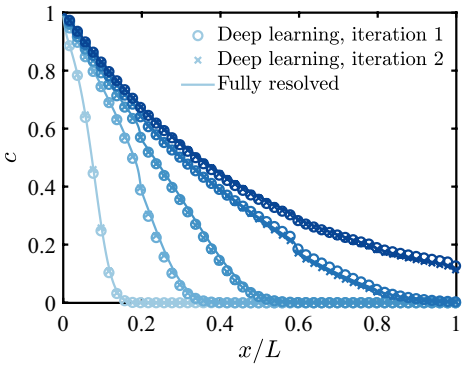

Figure 9. (a) Temporal snapshots of concentration at the centerline of the middle main fracture for the reactive transport case, at time instances 1,000 s, 3,000 s, 5,000 s, 10,000 s and 50,000 s (from light color to dark color).

where U_m is the maximum velocity and $H_m = 0.4$ mm is the maximum fracture aperture. The Pe value ensures the residence time is in hours, which is common in core-scale experiments, while the Da value ensures a concentration breakthrough can be observed at the outlet.

The case is solved by the deep leaning multiscale algorithm following the steps in Section 3.2. Two RNNs are constructed to predict the mass flux at microcrack inlets and outlets, each containing two hidden layers with 51 nodes in each layer. To generate the training set, 20 microcracks are selected uniformly in the fracture network. A test set is also introduced to prove that the training set is large enough and that there is no bias or overfitting in the training. The test set is generated by selecting four additional microcracks in the fracture network, whose inlets are located at $x = 1.64$, 17.94, 34.03, 50.33 mm. The first and third microcracks in the test set are selected from the bottom half of the fracture network, and the second and fourth are from the top half (Figure 1). The testing results are presented in Figure 8, where predictions of mass flux histories are marked by circles and reference values are plotted by solid lines. We define mass flux to be negative if solute transport is from the main fractures to microcracks. At the inlets, where microcracks are connected to the middle main fracture, the mass flux is alway negative, while at the outlets, where microcracks are connected to the bottom or the top main fractures, the mass flux may become slightly positive before switching to negative. This is because the middle main fracture always feeds solute into microcracks. The solute is mostly consumed in microcracks by reaction, but a small portion is able to move through to the bottom or top main fractures. Thus, the bottom and top main fractures can receive solute from microcracks, causing a slightly positive mass flux. We observe that the coupling between microcrack inlet and outlet as well as other nonlinear features can be accurately captured by the deep learning algorithm.

After proving the RNNs are well trained, the deep leaning multiscale algorithm is validated against fully resolved simulations. Figure 9 presents temporal snapshots of concentration profiles in the middle main fracture. Several iterations are performed in the deep learning multiscale modeling. Similar to the pure diffusion case, the error is small even with only one iteration, and the accuracy improves in the second iteration (Figure 10). No further improvements are observed in the third iteration, since the training set after the first iteration is already representative.

Both the deep learning multiscale modeling and the fully resolved simulation are performed on Intel Xeon Gold 6310 processor (2.1 GHz). To make computational time comparable, no parallel computation is implemented, although the training set generation can be easily parallelized due to the independence of the data. It takes 416 s to generate the training set, 772 s to train the RNNs, and 333 s to solve the transport in main fractures. Compared to the fully resolved simulation, which takes 18,776 s, the speedup factor is 12.3

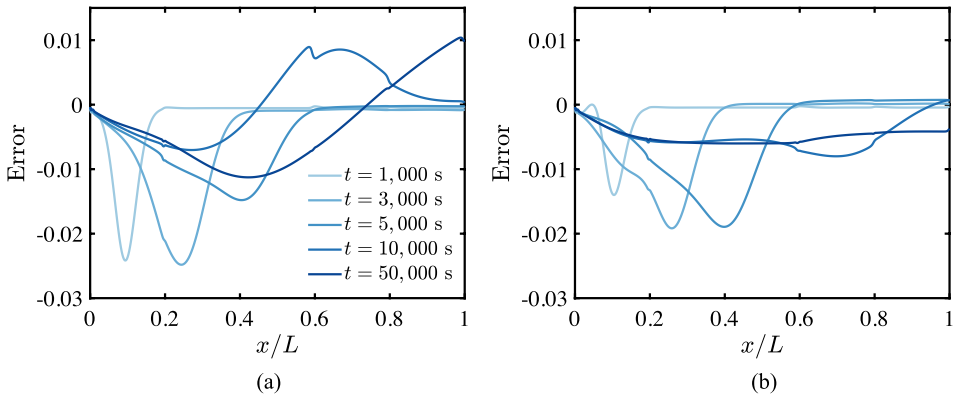

Figure 10. Normalized concentration differences between the deep learning multiscale modeling and fully resolved simulations for the reactive transport case: (a) iteration 1; (b) iteration 2.

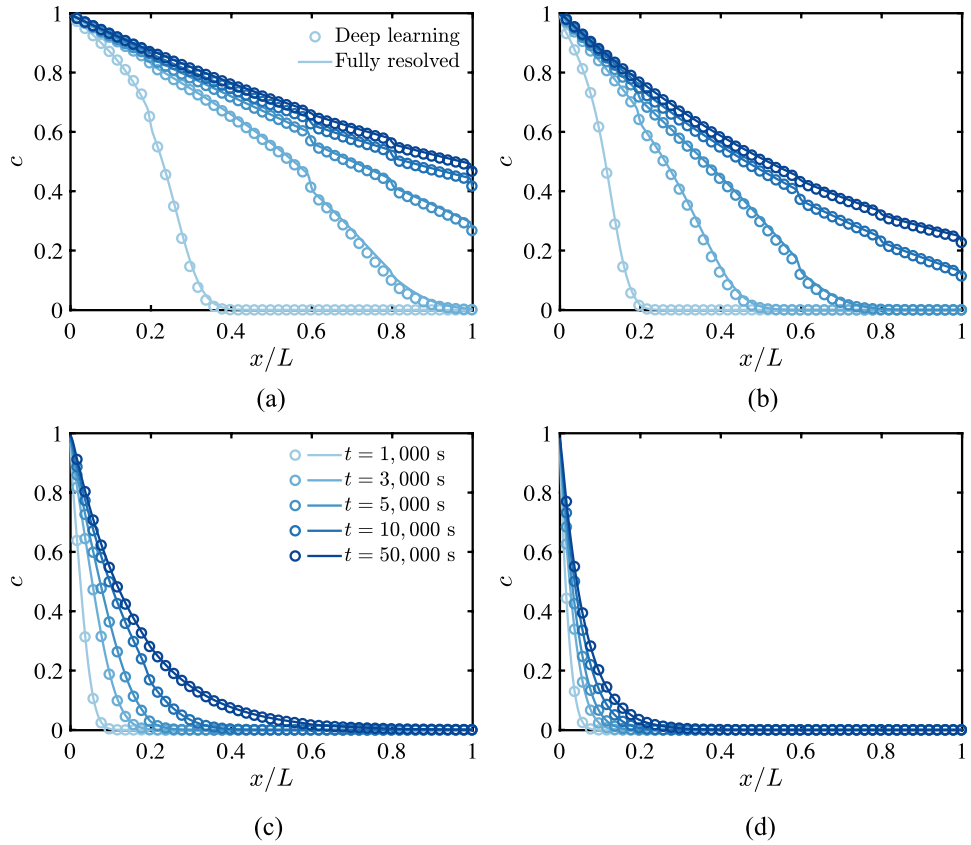

Figure 11. Temporal snapshots of concentration at the centerline of the middle main fracture for reactive transport cases with different *Pe*: (a) $Pe = 9.87$, (b) $Pe = 4.93$, (c) $Pe = 0.99$, (d) $Pe = 0.20$. The deep learning results are predicted by a general model that can work under various *Pe*.

if training is included, and 56.4 if a trained RNN is already available. This aspect will be further discussed next.

Training new RNNs for every new case is computationally expensive, however, it is possible to train a general model that can work under various conditions. Specifically, we construct a deep learning model that can work under various Péclet numbers (*Pe*). We start by considering five specific cases with $Pe = 6.58, 3.29, 1.64, 0.82, 0.41$ and solve each case following the steps in Section 3.2. When the training set is obtained with one iteration (i.e., go from step 1 to 7, then go from step 3 to 6), we generate a larger training set as the union of the training sets of each case, then train RNNs based on the new training set following step 7. The Péclet number mainly influences the concentration histories, and by expanding the training set, the RNN can predict the corresponding mass flux at different Péclet numbers. To validate the general model, we solve cases with new $Pe = 9.87, 4.93, 0.99, 0.20$ and compare the results with fully resolved simulations (Figure 11). The good agreement suggests that the general model can work under a wide range of *Pe*, including both advection dominated and diffusion dominated regimes. It also shows that the model can not only interpolate but also extrapolate over *Pe*.

4.3. Reactive Transport with Clogging

We solve the advection-reaction-diffusion problem with microcrack clogging in this section, that is, the solute consumed by reactions can form layered precipitates on microcrack walls. Equation 2 and Equation 3 are solved in the multiscale fracture network, under the same initial and boundary conditions given by Equation 8. We consider a specific case with $Pe = 6.58$ and $Da = 2 \times 10^{-3}$. The *Pe* and *Da* are selected so that most microcracks are fully clogged at the end of the simulation.

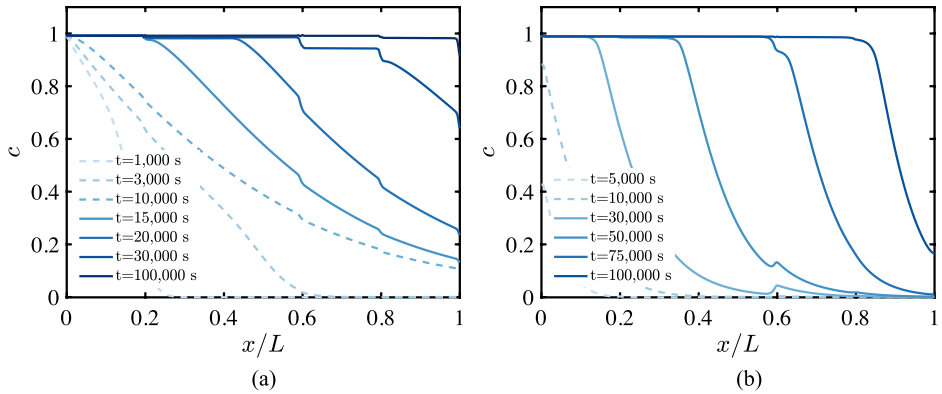

Figure 12. Temporal snapshots of concentration at the centerline of the (a) middle main fracture and (b) bottom main fracture. The dashed and solid lines are before and after the occurrence of the first complete clogging.

The implementation of microcrack clogging in the deep learning multiscale algorithm is straightforward. When modeling reactive transport in selected microcracks (step 5 in Section 3), the geometry is remeshed every time step to track the altered wall boundary (see Appendix A for details). Since the mass flux shows more complex patterns after clogging is introduced, a deeper RNN (four hidden layers) with more nodes (204 nodes in each hidden layer) is employed. The training set is generated by selecting 20 microcracks uniformly in the fracture network. To ensure convergence, the training data in the current iteration are combined with the data in the previous iteration, which is equivalent to adding a 0.5 relaxation factor. Figure 12 presents the modeling results: Concentration profiles in the middle main fracture and the bottom main fracture are plotted in Figures 12a and 12b, respectively. The dashed and solid lines are before and after the occurrence of the first complete clogging. We find that precipitation in microcracks can affect solute transport in main fractures in two ways. If the precipitation is faster than the transport, one concentration front is observed, which propagates as microcracks are getting clogged (Figure 12b). On the other hand, if the transport is faster than the precipitation, two concentration fronts are observed: the first front is caused by advective transport (dashed lines in Figure 12a), while the second is caused by microcrack clogging, which reduces the transport from main fractures to microcracks (solid lines in Figure 12a). The results in Figure 12 are obtained after four iterations, when the algorithm has already converged. Concentration profiles from previous iterations are also plotted in Figure 13, indicating that the deep learning multiscale algorithm converges quickly.

After convergence, the modeling is validated against a test set, which is generated by four microcracks at the same locations as in Section 4.2. Concentration breakthrough curves (i.e., concentration histories) at the inlets and outlets of these microcracks are presented in Figure 14a and 14b. The mass fluxes predicted by RNNs based on these curves, as well as reference data from pore-scale modeling, are plotted in Figure 14c

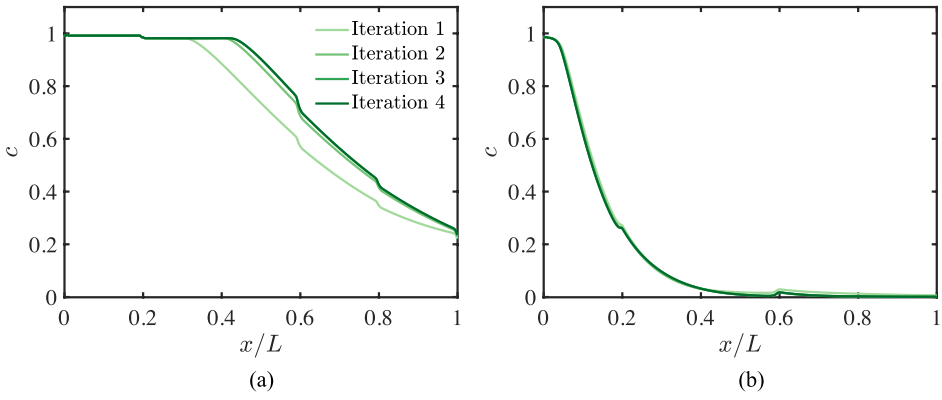

Figure 13. Concentration profiles at $t = 20,000$ s for the case with microcrack clogging: (a) in the middle main fracture and (b) in the bottom main fracture. The results from the first four iterations suggest a quick convergence.

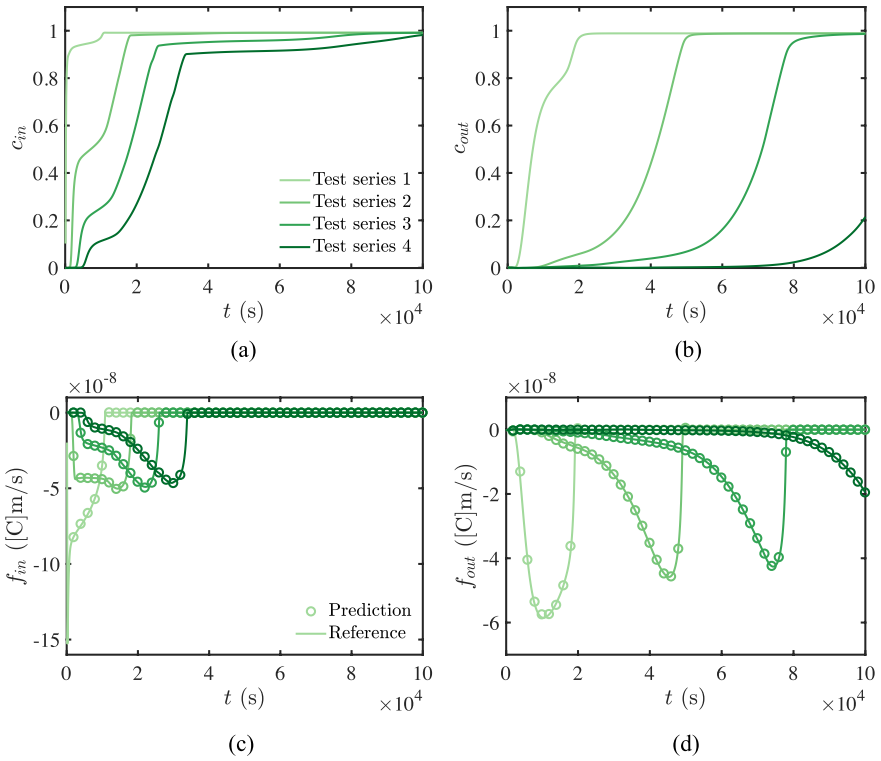

Figure 14. Concentration breakthrough curves (i.e., concentration histories) at (a) inlets and (b) outlets of the four microcracks in the test set, whose inlets are located at $x = 1.64, 17.94, 34.03, 50.33$ mm. The corresponding mass flux histories are plotted in (c) and (d), where circles are recurrent neural network (RNN) predictions and solid lines are reference data. The results are obtained after four iterations.

and 14d. Figure 15 tracks the evolution of precipitation thickness in a microcrack, whose inlet and outlet are both fully clogged durning the simulation. The results suggest the deep learning approach can accurately upscale reactive transport and clogging in microcracks.

5. Conclusions

Reactive transport and clogging in microcracks, which cannot be accurately described by traditional effective medium theory, is upscaled by deep learning. RNN is employed to predict the solute transport between main fractures and microcracks based on the concentration histories at microcrack inlets and outlets. In multiscale modeling, only main fractures are explicitly resolved while the solute transport to microcracks is modeled as a mass flux wall boundary condition, provided by deep learning. The deep learning approach is validated against fully resolved simulations and a steady-state analytical solution. The major conclusions of this work can be summarized as follows:

- The results of deep learning multiscale modeling agrees well with fully resolved simulations in the entire space and time domain.
- A general model is developed which can work over a wide range of *Pe*, including both advection dominated and diffusion dominated regimes.
- In the investigated case, the speedup factor (without parallel computation) is 12.3 if training is included, and 56.4 if a trained RNN is available, for example, using a general model. The speedup factor can be further improved for parallel implementation and larger fracture networks.

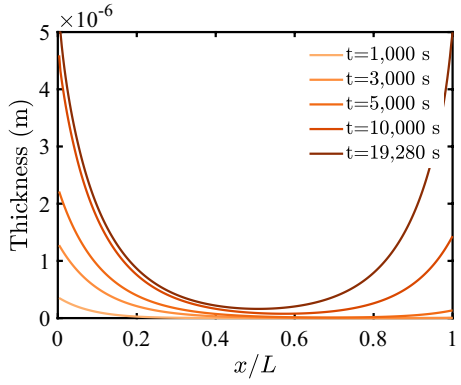

Figure 15. The evolution of precipitation thickness in the first microcrack in the test set, whose inlet is located at $x = 1.64$ mm.

In future works, geometric features of microcracks (e.g., length, aperture) will be included in the deep learning to generalize the approach. More complex reaction and precipitation models may also be incorporated into the deep learning framework.

Appendix A: Algorithm for Modeling Microcrack Clogging

The clogging in microcracks is modeled by interface tracking method. After the amount of precipitation is calculated in each time step, the geometry is remeshed to alter the wall boundary. We start by substituting Equation 3b into Equation 3a, which leads to:

$$-\mathbf{n} \cdot D\nabla c = Kc(1 - cV). \tag{A1}$$

We march Equation 2 with Equation A1 in a microcrack from t^n to t^{n+1} using the wall boundary position at t^n. The average concentration between t^n and t^{n+1} is:

$$c_{avg}(\mathbf{x}) = \frac{1}{2}[c(\mathbf{x}, t^n) + c(\mathbf{x}, t^{n+1})]. \tag{A2}$$

Then the increase of precipitation thickness is obtained by multiplying δt on both sides of Equation 3b to obtain

$$\delta s = K_c c_{avg} V \delta t. \tag{A3}$$

Since the microcrack has a large aspect ratio, we assume precipitation does not significantly change the normal direction of the wall boundaries. With this assumption, the new boundary position at t^{n+1} is tracked by Equation A3 and the geometry is remeshed accordingly. To prevent negative aperture, we define a small threshold ϵ, which is 0.1% of the microcrack aperture before clogging. The aperture cannot be smaller than the threshold during remeshing, and when such a value reached the fracture is considered fully clogged at the corresponding locations.

We adopt the clogging module in our previous work (Wang & Battiato, 2020) with the following improvements. First, the $\mathbf{u}\ c$ term in Equation 3a is commonly neglected in the literature when the interface velocity $\mathbf{u}$ is very small (X. Li et al., 2010; Mourzenko et al., 1996). However, Equation A1 indicates the contribution of the $\mathbf{u}\ c$ term is controlled by cV, which may not be neglected even if interface velocity $\mathbf{u}$ is very small. Hence, we adopt the complete wall boundary condition Equation 3 without neglecting any terms. Second, the time step for remeshing was 10 times as the simulation time step in our previous work, assuming the fracture aperture alteration is slow. Now the remeshing time step is the same as the simulation step to improve accuracy. Third, the reactive wall boundary condition was realized by "mixed" wall boundary scheme in OpenFOAM, which unintentionally changes reaction rate as grid size is changing. Now the reactive wall boundary condition is accurately implemented by the "coded mixed" scheme in OpenFOAM.

To demonstrate the improvements, we consider a benchmark problem in an isolated microcrack. The microcrack is uniformly saturated at the initial state, then solute gradually precipitates on the walls. With no flow and no mass flux boundary conditions at the inlet and outlet, the problem is analytically described by the following volume balance and mass balance equations:

$$-\frac{\partial h}{\partial t} = 2KcV, \tag{A4a}$$

$$-\frac{\partial (ch)}{\partial t} = 2Kc, \tag{A4b}$$

where concentration c and fracture aperture h depend only on time because we assume solute transport across the fracture is much faster than reaction due to the small fracture aperture. We compare the simulation results with the analytical solution of Equation A4 in Figure A1. After the improvements, the error is reduced to around 1% with the current simulation time step $\delta t = 10\ s$ and can be further reduced to 0.1% with $\delta t = 1\ s$, indicating the present model is accurate.

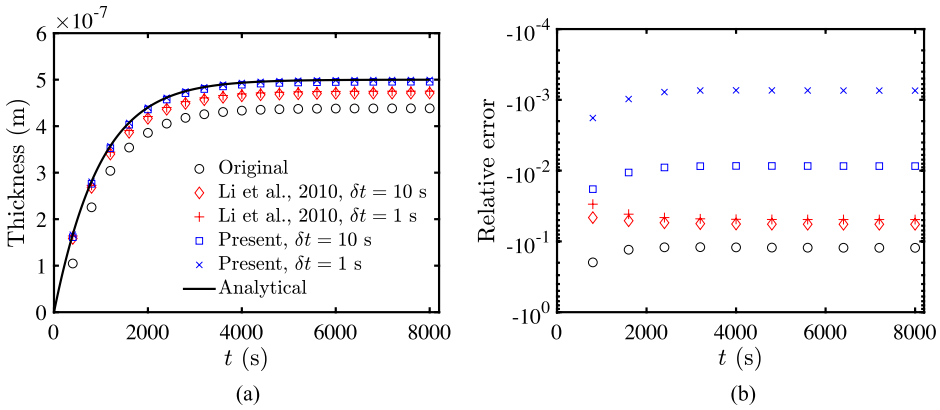

Figure A1. (a) Precipitation thickness over time in the benchmark problem. (b) Relative error of the simulation results compared to the analytical solution.

Data Availability Statement

All the synthetically generated data are available online (https://doi.org/10.4121/13138502).

Acknowledgments
This work was supported as part of the Center for Mechanistic Control of Water-Hydrocarbon-Rock Interactions in Unconventional and Tight Oil Formations (CMC-UF), an Energy Frontier Research Center funded by the U.S. Department of Energy, Office of Science under DOE (BES) Award DE-SC0019165.

References

Alalli, A., Li, Q., Jew, A., Kohli, A., Bargar, J., Zoback, M., & Kovscek, A. (2018). Effects of hydraulic fracturing fluid chemistry on shale matrix permeability. In *Unconventional resources technology conference* (pp. 808–817), Houston, TX. https://doi.org/10.15530/urtec-2018-2881314

Bao, J., Murugesan, V., Kamp, C. J., Shao, Y., Yan, L., & Wang, W. (2020). Machine learning coupled multi-scale modeling for redox flow batteries. *Advanced Theory and Simulations*, *3*. 1900167. https://doi.org/10.1002/adts.201900167

Battiato, I., Ferrero, V. P. T., O' Malley, D., Miller, C. T., Takhar, P. S., Valdés-Parada, F. J., & Wood, B. D. (2019). Theory and applications of macroscale models in porous media. *Transport in Porous Media*, *130*, 5–76. https://doi.org/10.1007/s11242-019-01282-2

Battiato, I., & Tartakovsky, D. M. (2011). Applicability regimes for macroscopic models of reactive transport in porous media. *Journal of Contaminant Hydrology*, *120*, 18–26. https://doi.org/10.1016/j.jconhyd.2010.05.005

Boso, F., & Battiato, I. (2013). Homogenizability conditions for multicomponent reactive transport. *Advances in Water Resources*, *62*, 254–265. https://doi.org/10.1016/j.advwatres.2013.07.014

Castanedo, F. (2013). A review of data fusion techniques. *The Scientific World Journal*, *2013*, 704504. https://doi.org/10.1155/2013/704504

Entrekin, S., Evans-White, M., Johnson, B., & Hagenbuch, E. (2011). Rapid expansion of natural gas development poses a threat to surface waters. *Frontiers in Ecology and the Environment*, *9*, 503–511. https://doi.org/10.1890/110053

Fleming, S. W., & Goodbody, A. G. (2019), A machine learning metasystem for robust probabilistic nonlinear regression-based forecasting of seasonal water availability in the US west, *IEEE Access*, *7*, 119943–119964. https://doi.org/10.1109/access.2019.2936989

Fleming, S. W., & Haggerty, R. (2001). Modeling solute diffusion in the presence of pore-scale heterogeneity: Method development and an application to the Culebra dolomite member of the Rustler formation, New Mexico, USA. *Journal of Contaminant Hydrology*, *48*, 253–276. https://doi.org/10.1016/s0169-7722(00)00182-0

Guo, B., Zeng, J., & Brusseau, M. L. (2020). A mathematical model for the release, transport, and retention of per-and polyfluoroalkyl substances (PFAS) in the vadose zone. *Water Resources Research*, *56*, e2019WR026. https://doi.org/10.1029/2019wr026667

Guo, T., Zhang, S., Qu, Z., Zhou, T., Xiao, Y., & Gao, J. (2014). Experimental study of hydraulic fracturing for shale by stimulated reservoir volume. *Fuel*, *128*, 373–380. https://doi.org/10.1016/j.fuel.2014.03.029

Haggerty, R., Fleming, S. W., Meigs, L. C., & McKenna, S. A. (2001). Tracer tests in a fractured dolomite: 2. Analysis of mass transfer in single-well injection-withdrawal tests. *Water Resources Research*, *37*, 1129–1142. https://doi.org/10.1029/2000wr900334

Hochreiter, S., & Schmidhuber, J. (1997). Long short-term memory. *Neural Computation*, *9*, 1735–1780. https://doi.org/10.1162/neco.1997.9.8.1735

Hornung, U. (1996). *Homogenization and porous media*. Springer Science & Business Media.

Kamrava, S., Tahmasebi, P., & Sahimi, M. (2020). Linking morphology of porous media to their macroscopic permeability by deep learning. *Transport in Porous Media*, *131*, 427–448. https://doi.org/10.1007/s11242-019-01352-5

Karpatne, A., Atluri, G., Faghmous, J. H., Steinbach, M., Banerjee, A., Ganguly, A., et al. (2017). Theory-guided data science: A new paradigm for scientific discovery from data. *IEEE Transactions on Knowledge and Data Engineering*, *29*, 2318–2331. https://doi.org/10.1109/tkde.2017.2720168

Khandelwal, A., Karpatne, A., Marlier, M. E., Kim, J., Lettenmaier, D. P., & Kumar, V. (2017). An approach for global monitoring of surface water extent variations in reservoirs using MODIS data. *Remote Sensing of Environment*, *202*, 113–128. https://doi.org/10.1016/j.rse.2017.05.039

Klie, M., & Florez, H. (2018). Data-driven modeling of fractured shale reservoirs. *ECMOR XVI-16th European conference on the mathematics of oil recovery* (pp. 1–18). European Association of Geoscientists & Engineers.

Kröner, E. (1986). Statistical modelling. In *Modelling small deformations of polycrystals* (pp. 229–291). Springer.

Li, Q., Jew, A. D., Kiss, A. M., Kohli, A., Alalli, A., Kovscek, A. R., et al. (2018). Imaging pyrite oxidation and barite precipitation in gas and oil shales. In *Unconventional resources technology conference* (pp. 875–884). Houston, TX. https://doi.org/10.15530/urtec-2018-2902747

Li, X., Huang, H., & Meakin, P. (2008). Level set simulation of coupled advection-diffusion and pore structure evolution due to mineral precipitation in porous media. *Water Resources Research*, *44*, W12407. https://doi.org/10.1029/2007wr006742

Li, X., Huang, H., & Meakin, P. (2010). A three-dimensional level set simulation of coupled reactive transport and precipitation/dissolution. *International Journal of Heat and Mass Transfer*, *53*, 2908–2923. https://doi.org/10.1016/j.ijheatmasstransfer.2010.01.044

Liu, D. C., & Nocedal, J. (1989). On the limited memory BFGS method for large scale optimization. *Mathematical Programming*, *45*, 503–528. https://doi.org/10.1007/bf01589116

Maloney, K. O., & Yoxtheimer, D. A. (2012). Production and disposal of waste materials from gas and oil extraction from the Marcellus Shale play in Pennsylvania. *Environmental Practice*, *14*, 278–287. https://doi.org/10.1017/s146604661200035x

Molson, J., Aubertin, M., & Bussière, B. (2012). Reactive transport modelling of acid mine drainage within discretely fractured porous media: Plume evolution from a surface source zone. *Environmental Modelling & Software*, *38*, 259–270. https://doi.org/10.1016/j.envsoft.2012.06.010

Mourzenko, V., Békri, S., Thovert, J., & Adler, P. M. (1996). Deposition in fractures. *Chemical Engineering Communications*, *148*, 431–464. https://doi.org/10.1080/00986449608936530

Ougier-Simonin, A., Renard, F., Boehm, C., & Vidal-Gilbert, S. (2016). Microfracturing and microporosity in shales. *Earth-Science Reviews*, *162*, 198–226. https://doi.org/10.1016/j.earscirev.2016.09.006

Parkhurst, D. L., & Appelo, C. (2013). *Description of input and examples for PHREEQC version 3: A computer program for speciation, batch-reaction, one-dimensional transport, and inverse geochemical calculations*. U. S. Geological Survey. https://doi.org/10.3133/tm6a43

Paukert Vankeuren, A. N., Hakala, J. A., Jarvis, K., & Moore, J. E. (2017). Mineral reactions in shale gas reservoirs: Barite scale formation from reusing produced water as hydraulic fracturing fluid. *Environmental Science and Technology*, *51*, 9391–9402. https://doi.org/10.1021/acs.est.7b01979

Santos, J. E., Xu, D., Jo, H., Landry, C. J., Prodanović, M., & Pyrcz, M. J. (2020). PoreFlow-Net: A 3D convolutional neural network to predict fluid flow through porous media. *Advances in Water Resources*, *138*, 103539. https://doi.org/10.1016/j.advwatres.2020.103539

Soulaine, C., & Tchelepi, H. A. (2016). Micro-continuum approach for pore-scale simulation of subsurface processes. *Transport in Porous Media*, *113*, 431–456. https://doi.org/10.1007/s11242-016-0701-3

Vidic, R. D., Brantley, S. L., Vandenbossche, J. M., Yoxtheimer, D., & Abad, J. D. (2013). Impact of shale gas development on regional water quality. *Science*, *340*, 1235009. https://doi.org/10.1126/science.1235009

Wang, Z., & Battiato, I. (2020). Patch-based multiscale algorithm for flow and reactive transport in fracture-microcrack systems in shales. *Water Resources Research*, *56*, e2019WR025. https://doi.org/10.1029/2019wr025960

Whitaker, S. (2013). *The method of volume averaging*. Springer Science & Business Media.

Wu, H., Fang, W., Kang, Q., Tao, W., & Qiao, R. (2019). Predicting effective diffusivity of porous media from images by deep learning. *Scientific Reports*, *9*, 1–12. https://doi.org/10.1038/s41598-019-56309-x

Yeh, G. T., Fang, Y., Zhang, F., Sun, J., Li, Y., Li, M. H., & Siegel, M. D. (2010). Numerical modeling of coupled fluid flow and thermal and reactive biogeochemical transport in porous and fractured media. *Computational Geosciences*, *14*, 149–170. https://doi.org/10.1007/s10596-009-9140-3